Preprint submitted to EarthArXiv

Overshoot pathway fingerprints persist after global temperature stabilization

Assaf Shmuel[1,2,*] Annika Högner[1,3], Niklas Schwind[1,3], Vassili Kitsios[4,5], Carl-Friedrich Schleussner[1,6]

[1] International Institute for Applied Systems Analysis (IIASA), Laxenburg, Austria

[2] Department of Geophysics, Tel Aviv University, Tel Aviv, Israel

[3] Geography Department, Humboldt University of Berlin, Berlin, Germany

[4] CSIRO Environment, 107-121 Station Street, Aspendale, 3195, Victoria, Australia

[5] Laboratory for Turbulence Research in Aerospace and Combustion, Department of Mechanical and Aerospace Engineering, Monash University, Clayton, 3800, Victoria, Australia

[6] Integrative Research Institute on Transformations of Human-Environment Systems (IRI THESys) and the Geography Department, Humboldt-Universität zu Berlin, Berlin, Germany

* Corresponding author: shmuel@iiasa.ac.at

Overshoot pathway fingerprints persist after global temperature stabilization

Assaf Shmuel[1,2,*] Annika Högner[1,3], Niklas Schwind[1,3], Vassili Kitsios[4,5], Carl-Friedrich Schleussner[1,6]

[1] International Institute for Applied Systems Analysis (IIASA), Laxenburg, Austria

[2] Department of Geophysics, Tel Aviv University, Tel Aviv, Israel

[3] Geography Department, Humboldt University of Berlin, Berlin, Germany

[4] CSIRO Environment, 107-121 Station Street, Aspendale, 3195, Victoria, Australia

[5] Laboratory for Turbulence Research in Aerospace and Combustion, Department of Mechanical and Aerospace Engineering, Monash University, Clayton, 3800, Victoria, Australia

[6] Integrative Research Institute on Transformations of Human-Environment Systems (IRI THESys) and the Geography Department, Humboldt-Universität zu Berlin, Berlin, Germany

* Corresponding author: shmuel@iiasa.ac.at

Abstract

Exceedance of global warming thresholds under overshoot, peak and decline pathways may leave regional climate legacies that persist even after global temperature stabilization. This study examines whether such overshoot pathway fingerprints remain detectable after stabilization at similar global warming levels by comparing two multi-century CMIP6 simulations with different magnitudes and characteristics of temperature exceedance. Using machine learning classifiers and statistical tests on regional multivariate climate data, we show that overshoot pathways leave detectable regional fingerprints. Regional climate states remain distinguishable between pathways, even when global temperatures stabilize. Comparisons with transient pre-overshoot periods at similar global warming levels further indicate that some regional differences will not reverse to their transient pre-exceedance state. These findings underline that the consequences of overshoot pathways cannot be assessed from global mean temperature trajectories alone. Evaluating possible impacts and risks from temporary exceedance of global warming of 1.5 °C requires attention to persistent regional fingerprints, including changes in the distribution and spatial structure of climate variables after stabilization.

Introduction

2024 was the first year in which global mean temperature reached 1.5 °C. This most likely signals that Earth is within the 20-year period that will reach the Paris Agreement temperature limit (1). Overshoot, peak and decline pathways have become central to mitigation and impact assessment because their risks may persist even if warming later declines (2–5). Yet, overshoot pathways are not simply a delayed route to the same climate outcome. Global and regional climate risks after overshoot pathways can differ from those in a world that avoids them, and confidence in the reversibility of impacts after returning global warming to 1.5 °C may therefore be misplaced (2).

Regional climate signals emerge and stabilize at different times because of differences in internal variability, feedbacks, and adjustment timescales (6–8). Stabilization simulations show that regional temperature, precipitation, sea ice, and variability can continue to evolve long after emissions cease, so stabilized climates need not resemble transient climates at the same global warming level (9). Overshoot pathway studies further show that regional temperature, precipitation, and extremes may reverse only partially after peak warming, with path dependence linked to ocean heat uptake, hemispheric temperature asymmetry, ITCZ shifts, cryospheric change, aerosols, and regional thermal inertia (10–14). Temporary exceedance of temperature limits also increases the risk for potentially irreversible non-linear shifts in the Earth system (15). Recent work comparing SSP1-2.6 and SSP5-3.4OS further shows that overshoot amplitude affects regional climate, with larger overshoots producing stronger hemispheric temperature contrasts and regional precipitation changes even after global temperature returns toward a common level (16).

Here we ask whether such pathway dependence remains detectable after late-period stabilization. Using long ACCESS-ESM-1.5 CMIP6 simulations through 2300 (17), we compare ensembles of a high-overshoot pathway, SSP5-3.4OS, and a low-overshoot pathway, SSP1-2.6, across AR6 reference regions (18–20). We examine near-surface air temperature, daily maximum and minimum near-surface air temperature, precipitation, and near-surface wind speed. We test three related questions: whether states of the climate system towards global temperature

stabilization differ between pathways, whether regional climates continue changing within each pathway, and whether pre- and post-peak states at similar global mean temperature are regionally equivalent.

We address these questions by comparing regional climate states in terms of both their distributions and spatial organization. This allows us to test whether late-period regional climate states are equivalent across pathways, or whether they remain distinguishable in ways that reflect the forcing history.

Methods

Data and regional preprocessing

We analysed monthly CMIP6 output from the ACCESS-ESM-1.5 model (17) for five climate variables: near-surface air temperature (tas), daily maximum near-surface air temperature (tasmax), daily minimum near-surface air temperature (tasmin), precipitation (pr), and near-surface wind speed (sfcWind). Analyses were performed separately for AR6 reference regions (20). Both land and ocean regions were analysed, although some figures present the land-only subset.

For each experiment, we compared two 20-year climate states. The five experiments were as follows:

Overshoot pathway fingerprint: SSP5-3.4OS in 2281-2300 (Window #3) was compared with SSP1-2.6 in 2281-2300. This tests whether the high-overshoot pathway state differs from a low-overshoot pathway state over the same late-period interval.

SSP1-2.6 stabilization: SSP1-2.6 in 2241-2260 (Window #2) was compared with SSP1-2.6 in 2281-2300 (Window #3). This tests the extent to which regional climates remain stable within the SSP1-2.6 pathway during the 23rd century.

SSP5-3.4OS stabilization: SSP5-3.4OS in 2241-2260 (Window #2) was compared with SSP5-3.4OS in 2281-2300 (Window #3). This tests the extent to which regional climates remain stable within the SSP5-3.4OS pathway during the 23rd century.

SSP1-2.6 reversibility: A pre-peak SSP1-2.6 window (Window #1) was selected to match the global-mean temperature of SSP1-2.6 in 2281-2300 (Window #3) and was then compared with SSP1-2.6 in 2281-2300 (Window #3).

SSP5-3.4OS reversibility: A pre-peak window (Window #1) was selected to match the global-mean temperature of SSP5-3.4OS in 2281-2300 (Window #3) and was then compared with SSP5-3.4OS in 2281-2300 (Window #3). Because SSP5-3.4OS branches from SSP5-8.5, the candidate pre-peak trajectory used SSP5-8.5 before 2041 and SSP5-3.4OS from 2041 onward.

For the reversibility experiments, the pre-peak comparison window was not fixed by calendar year. Instead, we computed the ensemble-mean global-mean temperature trajectory using tas, then selected the 20-year pre-peak window whose mean global temperature was closest to the mean global temperature of the 2281-2300 target window. The same resolved window was then used for all variables, so that reversibility was evaluated at approximately matched global-mean temperature rather than at an arbitrary earlier date. We use CO_2 data per scenario (21) for illustrative purposes.

To assess whether the ACCESS-ESM-1.5 results were sensitive to structural model uncertainty, we also performed a multi-model sensitivity analysis using one available member per CMIP6 model for models with simulations extending to 2300. This analysis used the same regional preprocessing, comparison windows, and statistical tests as the main ACCESS-ESM-1.5 analysis, but excluded the machine-learning classifier because the grouped cross-validation framework requires multiple ensemble members from the same model. The multi-model analysis was therefore used as a statistical sensitivity check rather than as a direct replication of the ensemble-based machine-learning framework. We used one available member from each CMIP6 model for which the relevant variables and scenario simulations were available through 2300: ACCESS-ESM-1.5 (17), CanESM5 (22), CESM2-WACCM (23), EC-Earth3-Veg (24), GISS-E2-1-G (25), GISS-E2-1-H (25), GISS-E2-2-G (26), IPSL-CM6A-LR (27), MIROC-ES2L (28), MRI-ESM2-0 (29), and UKESM1-0-LL (30).

Distributional tests

For each AR6 region, variable, and experiment, we compared the distributions of annual values from all simulations of the two 20-year periods relevant for the experiment (labeled A and B) using two complementary two-sample tests. First, we used a two-sided Kolmogorov-Smirnov test to detect differences in the full distribution of annual regional values, rather than only differences in the mean (7, 9). Second, we used a Mann-Whitney U-test to assess whether values from one window tended to be systematically larger or smaller than values from the other window, without assuming normally distributed samples (31). Finally, we used a Welch two-sample t-test to test for differences in the mean while allowing unequal variances. Because Welch's t-test assumes approximately normally distributed samples, results from this test are presented in the Supplementary Information and used as a sensitivity check rather than as the primary distributional evidence. All three tests were applied to annual regional samples from the same A and B windows.

In addition to the distributional testing, we assign the direction of change using the sign of the mean difference, A minus B. For member-wise analyses, the test was applied separately to each ensemble member, and regional significance was summarized across members. Directional robustness was quantified by the fraction of members agreeing on the sign of the A minus B mean difference. A region was classified as a robust increase or decrease only when the statistical test was significant, and the member-wise sign agreement exceeded a 60% threshold.

Machine-learning distinguishability

As a complementary pattern-based measure of regional distinguishability, we trained binary classifiers to distinguish samples from windows A and B (32). For each AR6 region, the classifier was trained separately using gridded values within that region as predictors. In the monthly-feature configuration, each sample corresponded to one ensemble-member year, and each regional grid cell contributed 12 monthly features. The main classifier used is LightGBM (33), trained as a binary model with labels indicating whether each sample came from window A or window B. Model performance was evaluated using grouped cross-validation by ensemble member, so that all samples from a given member were assigned to the same fold and were not split between training and validation sets. The primary performance metric was the

receiver operating characteristic area under the curve (ROC AUC), which measures how well the classifier ranks samples from the two windows across all possible classification thresholds (34) and is commonly used in classification benchmarks (35, 36). An AUC of 0.5 indicates no better-than-random discrimination, while an AUC of 1 indicates perfect separation. AUC values significantly above 0.5 (where "significant" accounts for the finite ensemble size) indicate that the two climate states are distinguishable from regional spatial patterns.

For monthly feature experiments, each regional grid cell contributed one feature per calendar month. To reduce dimensionality and computational cost, fields were regridded or coarsened to a 5° latitude-longitude grid before classification. For each experiment, variable, and region, we recorded cross-validated AUC and permutation-based p-values for AUC. The permutation test was repeated 20 times by randomly shuffling the A/B labels and recomputing the cross-validated AUC, providing a null distribution against which the observed AUC was compared. The ML analysis therefore tested whether regional spatial patterns contain enough information to distinguish the two climate states, while the KS and Mann-Whitney analyses tested distributional or rank-based differences in annual regional values, and the Welch t-test tested mean differences.

The different methods are summarized in Table 1.

Table 1. Summary of the detection methods used in the study.

Method	What it tests	Null hypothesis	Assumes normality?	Role in paper
Machine learning	Whether regional climate fields from window A and window B are distinguishable	A classifier cannot distinguish the two windows better than chance	No	Machine-learning detection of separability between windows, evaluated with grouped cross-validation by ensemble member
Mann-Whitney U test	Whether values in one window tend to be larger or smaller than values in the other	The two windows have the same rank distribution	No	Non-parametric test for distributional or rank shifts
Kolmogorov-Smirnov test	Whether the full distributions differ	The two windows are drawn from the same distribution	No	Primary distributional test
Welch two-sample t-test	Whether the mean differs between windows	Mean(A) = Mean(B)	Yes	Parametric sensitivity test for mean shifts

Summary and visualizations

For each method, results were summarized by counting the number of AR6 regions showing robust increases, robust decreases, non-robust changes, or no significant change. Summary bar plots were produced for all AR6 regions and land-only regions. Maps show the regional significance category for each variable and experiment using a five-variable panel layout, allowing comparison across variables and experiments.

Fig. 1 summarizes the study design. We compare late-period differences between pathways, continued change within each pathway, and reversibility between pre- and post-peak states at a similar global mean temperature. Together, these comparisons test whether regional climates converge after stabilization or retain detectable memory of the pathway.

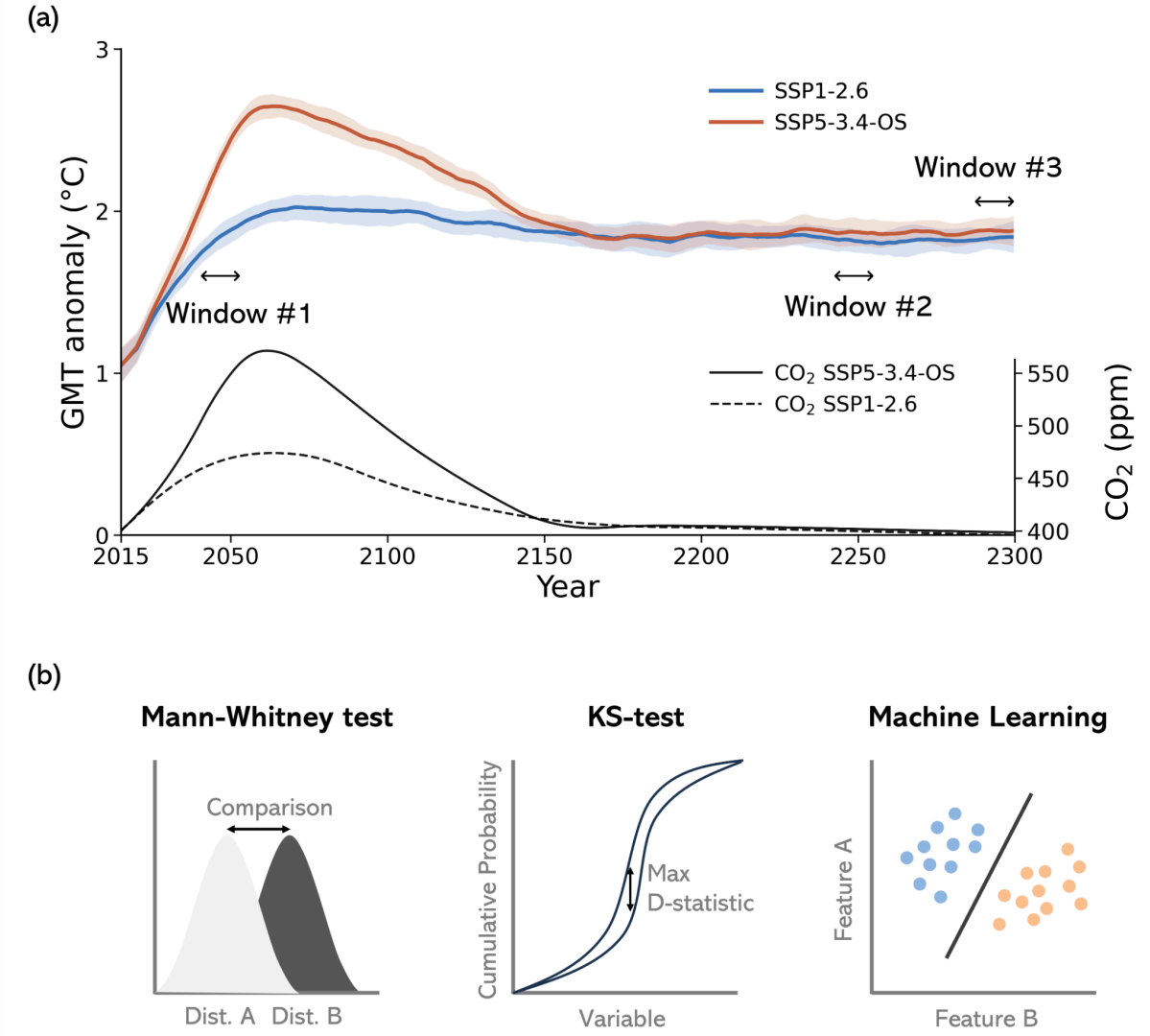

Fig. 1. Study design and statistical framework. *(a) Global mean temperature trajectories and the comparison windows used to test overshoot pathway fingerprints, stabilization, and reversibility. (b) Regional climate states are then compared using the Mann-Whitney test and Kolmogorov-Smirnov test for distributional shifts, and machine-learning classifiers for spatial-pattern distinguishability.*

Results

Across the five experiments, the three diagnostics give a consistent but method-dependent picture of pathway memory, late-period stabilization, and

reversibility. The machine-learning classifier is generally the most sensitive diagnostic, because it tests whether regional spatial patterns distinguish the two climate states. The Kolmogorov-Smirnov and Mann-Whitney tests are more conservative, because they test differences in regional annual distributions or ranks.

Global-mean near-surface temperature does not differ significantly between 2241 to 2260 and 2281 to 2300 in either SSP1-2.6 or SSP5-3.4OS under the Kolmogorov-Smirnov and Mann-Whitney tests. This indicates that these late-period windows are broadly comparable in global temperature and can be considered stabilized in terms of their global temperature outcome (16).

In the overshoot pathway fingerprint experiment, SSP5-3.4OS and SSP1-2.6 remain distinguishable in the late 23rd century across all five variables, although the strength and direction of the signal differ by variable and method (Fig. 2). Machine-learning distinguishability is widespread, indicating that regional spatial patterns retain information about the pathway even after global temperature stabilization. The KS and Mann-Whitney tests show fewer robust changes than the machine-learning classifier, but they still identify significant and robust regional differences for several variables and regions. This indicates that the late-period overshoot pathway fingerprint is not only a spatial-pattern effect, but in some regions is also expressed as a shift in regional distributions or ranks. The same comparison with non-significant and non-robust sign categories separated is shown in Fig. S1, and the corresponding all-region version including oceans is shown in Fig. S2.

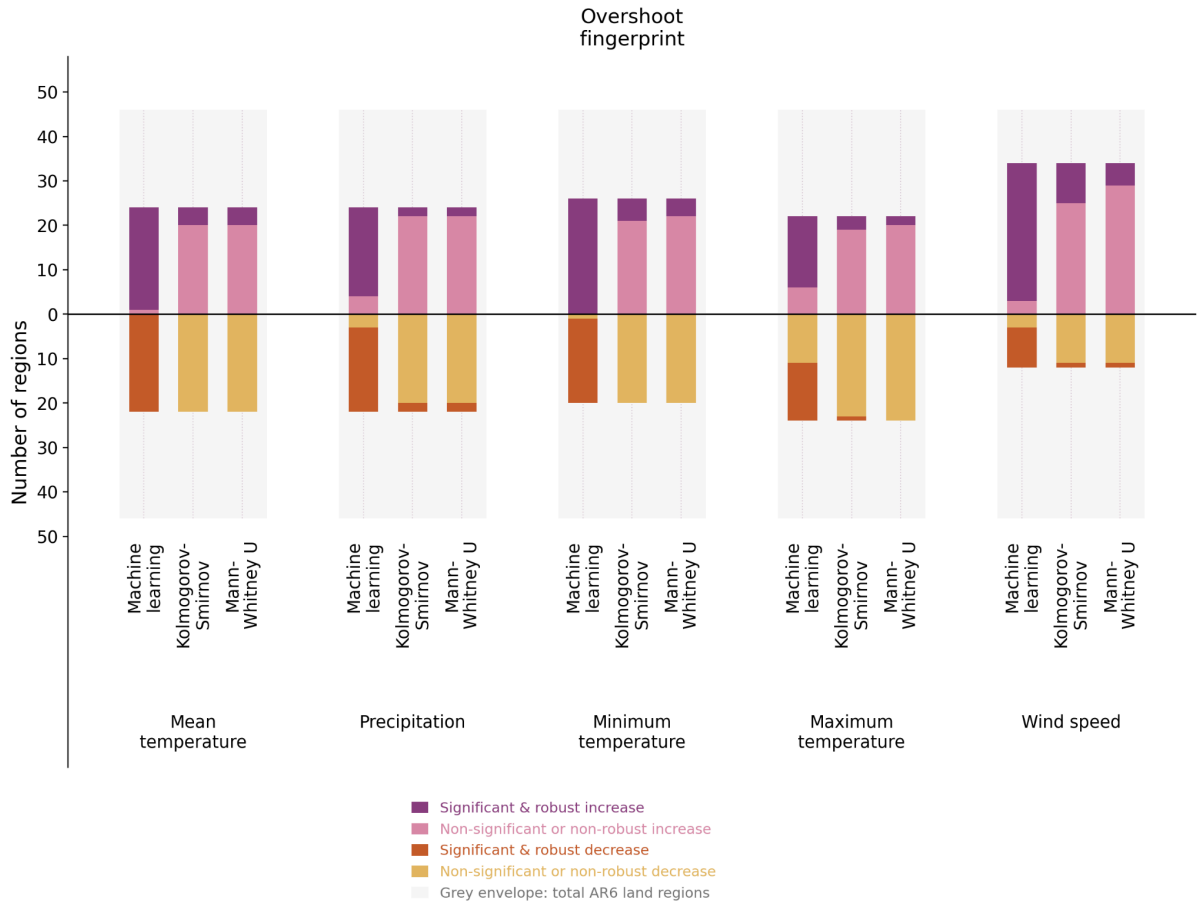

Fig. 2. Overshoot pathway fingerprint in late-period regional climate states. *Number of AR6 land regions showing regional climate-state differences between SSP5-3.4OS and SSP1-2.6 in 2281 to 2300. Results are shown for five climate variables and three diagnostics: machine-learning classification, the two-sample Kolmogorov-Smirnov test, and the Mann-Whitney U-test. Positive bars indicate regions where the A minus B mean difference is positive, and negative bars indicate regions where the A minus B mean difference is negative. Dark colors show statistically significant and directionally robust increases or decreases, while lighter colors show non-significant or non-robust changes. Grey envelopes indicate the total number of available AR6 land regions. The comparison tests whether regional climates reached through a high-overshoot pathway remain distinguishable from those reached through a lower-overshoot pathway after late-period global temperature stabilization.*

The within-pathway stabilization experiments show a different pattern (Fig. 3). For both SSP1-2.6 and SSP5-3.4OS, most regions fall into non-significant or non-robust categories for the KS and Mann-Whitney tests, indicating that late-period regional distributions are mostly stable between 2241 to 2260 and 2281 to 2300. Machine-learning distinguishability remains somewhat present in some variables and

regions, especially for temperature variables, suggesting that residual adjustment can persist in regional spatial patterns even when regional distributions show limited robust change. The two stabilization experiments do not provide clear evidence that late-period regional stationarity is systematically stronger in SSP1-2.6 than in SSP5-3.4OS. Instead, both pathways show broadly limited but nonzero residual change during the late 23rd century. The separated category versions of these stabilization summaries are shown in Fig. S3 for land regions and Fig. S4 when ocean regions are included.

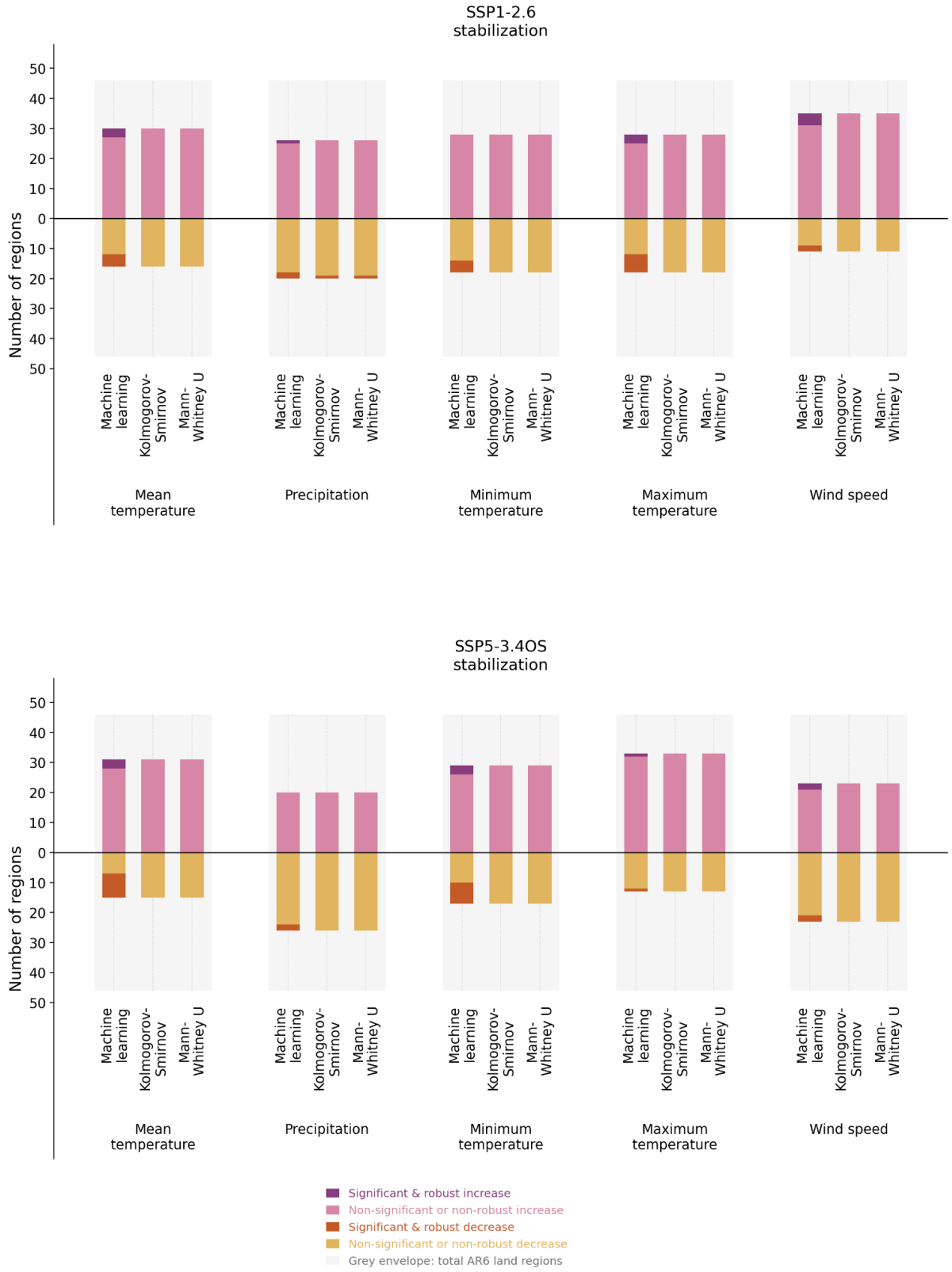

Fig. 3. Late-period stabilization within SSP1-2.6 and SSP5-3.4OS. *Number of AR6 land regions showing regional climate-state differences between 2241 to 2260 and 2281 to 2300 within each pathway. The upper panel shows SSP1-2.6 and the lower panel shows SSP5-3.4OS. For each variable, machine-learning classification, the Kolmogorov-Smirnov test, and the Mann-Whitney U-test*

are shown side by side. Positive and negative bars indicate the direction of the A minus B mean difference, with dark colors denoting statistically significant and directionally robust changes and lighter colors denoting non-significant or non-robust changes. Grey envelopes indicate the total number of available AR6 land regions. These comparisons test whether regional climate states continue to evolve during the late 23rd century after apparent global temperature stabilization.

The matched-global-temperature reversibility comparisons show the strongest and most widespread separation between climate states (Fig. 4). In both SSP1-2.6 and SSP5-3.4OS, pre-peak and late-period regional climates remain widely distinguishable despite having similar global mean temperatures. This separation is strongest for the machine-learning classifier, which identifies widespread regional separability across temperature variables, precipitation, and wind speed. The KS and Mann-Whitney tests also show substantial numbers of robust regional differences, especially for precipitation and temperature-related variables. These results show that matching global mean temperature is not sufficient to ensure regional climate-state equivalence. Because the pre-peak windows occur during transient warming, the differences should not be interpreted as direct proof of hysteresis on their own. They are nevertheless consistent with regional path dependence and show that late-period regional climate states cannot be inferred from global mean temperature alone. The corresponding separated-category reversibility summaries are shown in Fig. S5 for land regions and Fig. S6 when ocean regions are included.

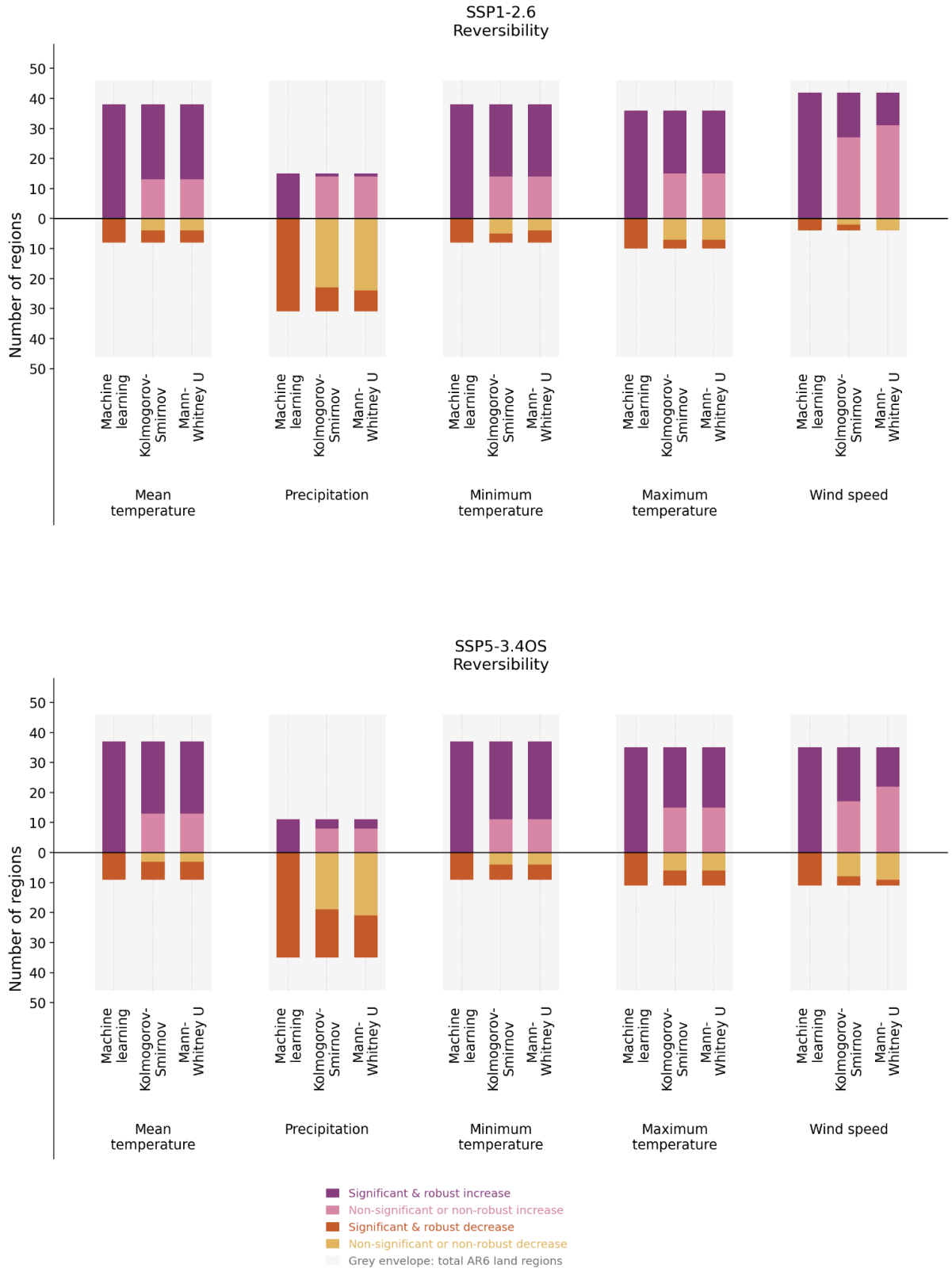

Fig. 4. Reversibility at matched global mean temperature. *Number of AR6 land regions showing differences between pre-peak and late-period climate states selected to have approximately matched global mean temperature. The upper panel shows SSP1-2.6 and the lower panel shows SSP5-3.4OS. Results are shown for five climate variables and three diagnostics: machine-learning classification, the*

Kolmogorov-Smirnov test, and the Mann-Whitney U-test. Positive and negative bars indicate the direction of the A minus B mean difference, with dark colors denoting statistically significant and directionally robust changes and lighter colors denoting non-significant or non-robust changes. Grey envelopes indicate the total number of available AR6 land regions. These comparisons test whether regional climates after stabilization resemble earlier climate states at the same global warming level, or whether they retain path-dependent differences after peak warming.

To assess whether the main findings were specific to the ACCESS-ESM-1.5 ensemble, we also performed a multi-model sensitivity analysis using one available member per model. This analysis provides an independent check on the statistical results across a broader set of models. Because the machine-learning analysis requires multiple ensemble members for grouped cross-validation, it is excluded from this analysis. The multi-model analyses are shown in Fig. S7 for the overshoot pathway fingerprint experiment, Fig. S8 for the stabilization experiments, and Fig. S9 for the reversibility experiments.

The regional maps of the overshoot pathway fingerprint experiment show that late-period pathway distinguishability is widespread but spatially heterogeneous (Fig. 5). For several variables, classifiers achieve high ROC AUC values across many AR6 land regions, indicating that regional spatial patterns contain information that separates SSP5-3.4OS in 2281 to 2300 from SSP1-2.6 over the same period. The corresponding permutation-based p-values show that this distinguishability is statistically strongest in a subset of regions rather than uniformly significant everywhere. This pattern indicates that the late-period overshoot pathway fingerprint is not simply a global or spatially uniform offset, but is expressed through regionally varying differences in the spatial structure of climate fields.

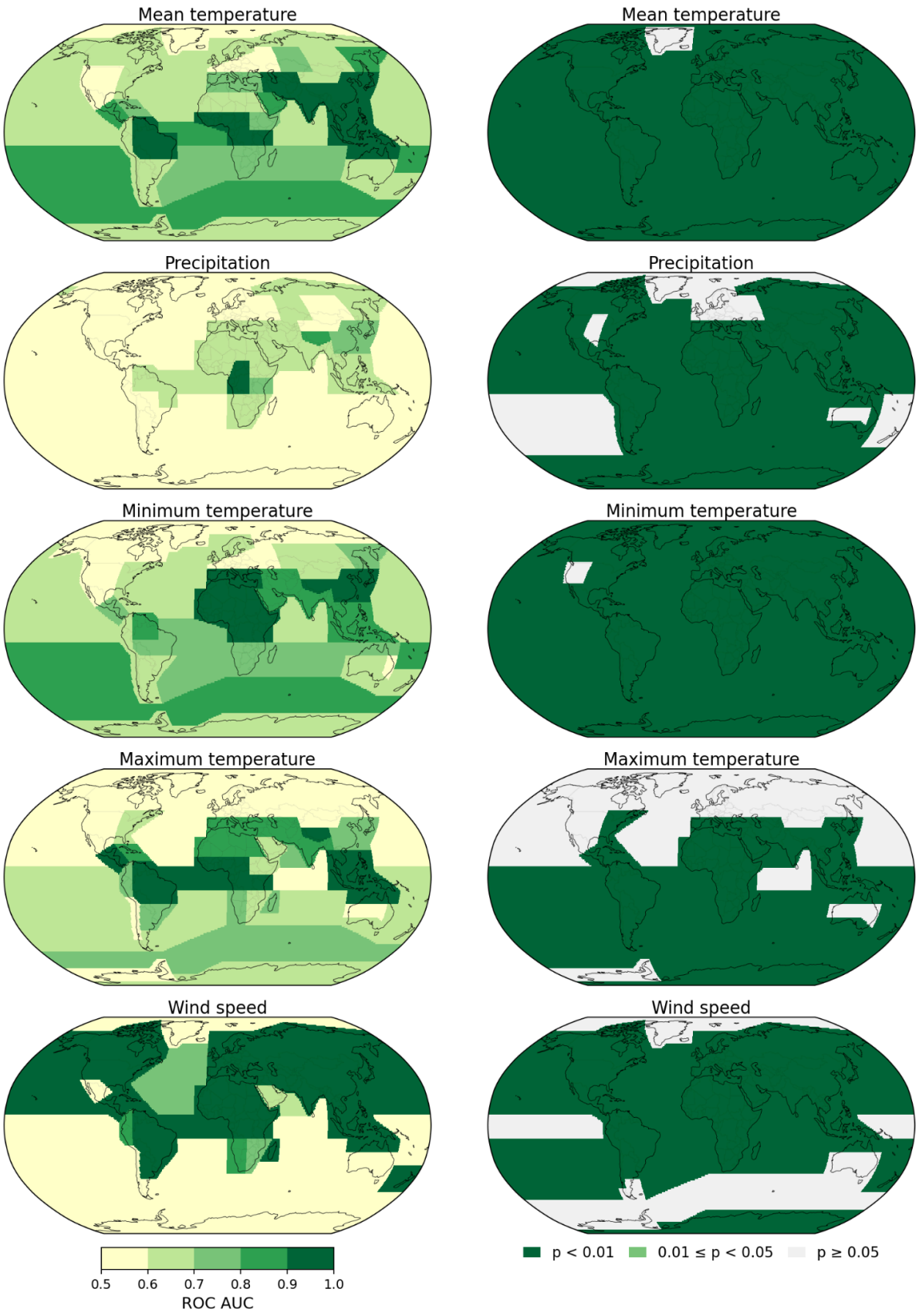

Fig. 5. Regional machine-learning performance for the overshoot pathway fingerprint experiment. *ROC AUC (left column) and permutation-based p-values (right column) for machine*

learning in the overshoot pathway fingerprint experiment, shown separately for each climate variable. Dark green regions indicate high ROC AUC (left column) and low p-values (right column).

The within-pathway stabilization maps provide little evidence that late-period stabilization is more complete in SSP1-2.6 than in SSP5-3.4OS (Figs. S10 and S11). If anything, the SSP1-2.6 comparison shows equal or greater residual distinguishability in several regions and variables, suggesting that the low-overshoot pathway is not necessarily more regionally stationary over the late 23rd century. This indicates that apparent stabilization of the global trajectory does not translate uniformly into stationary regional spatial patterns, even in the lower-emissions scenario.

The matched-global-temperature reversibility maps show that the contrast between pre-peak and late-period climates is spatially widespread in both pathways (Figs. S12 and S13). Regional classifiers distinguish the late-period state from the earlier pre-peak state across most regions and variables, with stronger and more spatially coherent distinguishability than in the within-pathway stabilization maps. These maps reinforce the summary results by showing that the reversibility signal is not confined to a small number of regions or variables.

Discussion

This study shows that climate stabilization at similar warming levels does not necessarily imply reversibility. Even after global temperature has approximately stabilized, regional climates reached through different forcing histories can retain detectable pathway memory. Across variables and regions, SSP5-3.4OS and SSP1-2.6 often differ not only in regional distributions but also in spatial patterns within AR6 regions. The matched-global-temperature comparisons further suggest that many regional differences cannot be explained by global mean temperature alone. Instead, regional climate states may depend on whether a given level of warming is reached before or after the peak of an overshoot pathway.

The diagnostics capture different aspects of regional climate-state separation. KS and Mann-Whitney test changes in regional distributions or ranks, whereas the

machine-learning classifier tests whether spatial patterns within a region distinguish the two states. This explains why ML distinguishability can be more widespread than distributional significance. Cases that are statistically significant but lack robust sign agreement should be interpreted cautiously: for example, a 20-year window affected by decadal variability could produce a significant regional distributional difference in some ensemble members, while other members show the opposite sign of change. Such cases indicate separability between samples, but not necessarily a directionally consistent forced response.

Several mechanisms may help explain why regional climate states remain distinguishable after global temperature stabilization. First, ocean adjustment occurs on longer timescales than global surface temperature, so heat uptake, heat redistribution, and circulation recovery can leave persistent regional anomalies (37, 38). This is especially relevant for high-latitude ocean regions, where previous studies show persistent North Atlantic and Southern Ocean warming after global temperature returns to a target level (37). More generally, deep-ocean heat uptake can modulate late-century and post-net-zero surface temperature trajectories, providing a physical basis for continued regional adjustment after apparent global stabilization (39).

Atmospheric circulation and aerosol forcing may also contribute to the regional structure of the fingerprints. Overshoot pathway and CO_2-removal experiments have shown pathway-dependent shifts in the ITCZ, Hadley circulation, ENSO behavior, and monsoon area, all of which can alter regional climates even when global temperature is similar between periods (40–44). In addition, aerosol reductions can produce strongly regional climate responses, especially near major historical aerosol-emission regions, and may be relevant for interpreting differences over East and South Asia in the reversibility comparisons (45, 46). These processes suggest that the fingerprints detected here are unlikely to reflect a single uniform offset, but rather a combination of ocean-memory, circulation-adjustment, and forcing-composition effects.

These findings are consistent with previous work showing that overshoot pathway impacts may be only partially reversible (2, 10, 16). Pfleiderer et al. showed that regional temperature, precipitation, and extremes do not always reverse with

declining global mean temperature (10), while Roldán-Gómez et al. linked post-overshoot irreversibility to hemispheric temperature asymmetry, ITCZ shifts, regional thermal inertia, aerosols, cryospheric change, and ocean heat transport (11). Our results extend this literature by focusing on late-period stabilization and by evaluating whether regional climates remain distinguishable as overall climate states, rather than assessing only the reversal of regional mean changes. They also align with stabilization studies showing that regional climate variables can continue to evolve after global forcing or temperature has stabilized (6, 9, 47).

Several limitations should be noted. First, the ensemble-based machine-learning analysis is limited to ACCESS-ESM-1.5 (17), because this was the only model with sufficient ensemble members for grouped cross-validation. To partly assess robustness across structural model uncertainty, we therefore complemented the ACCESS-ESM-1.5 analysis with a multi-model sensitivity analysis using one available member per model. This multi-model analysis supports the statistical interpretation of the results, but it does not provide a direct replication of the machine-learning framework. Second, the comparison between the 23rd-century state and the pre-peak window should be interpreted with caution, because the pre-peak window occurs during a transient warming period rather than under approximately stabilized climate conditions. Next, machine-learning distinguishability indicates that regional spatial patterns contain information about pathway or period, but it does not by itself identify the physical mechanisms responsible for the difference or its impact relevance. Finally, the analysis focuses on selected atmospheric variables and could be expanded to additional variables in future work.

Overall, the results suggest that risks associated with overshoot pathways cannot be assessed from global mean temperature trajectories alone. Even after apparent stabilization, regional climate distributions and spatial structures may retain detectable memory of the forcing pathway. Assessing the consequences of overshoot pathways therefore requires attention not only to how high global temperature rises and when it returns, but also to the regional climate states left behind.

Acknowledgements

A.S. acknowledges fellowship support from the Council for Higher Education Energy and Climate Postdoctoral Fellowship.

Conflicts of interest

The authors declare no conflicts of interest.

Data availability statement

All datasets used in this study are publicly available from the sources cited in the manuscript.

Supplementary Information

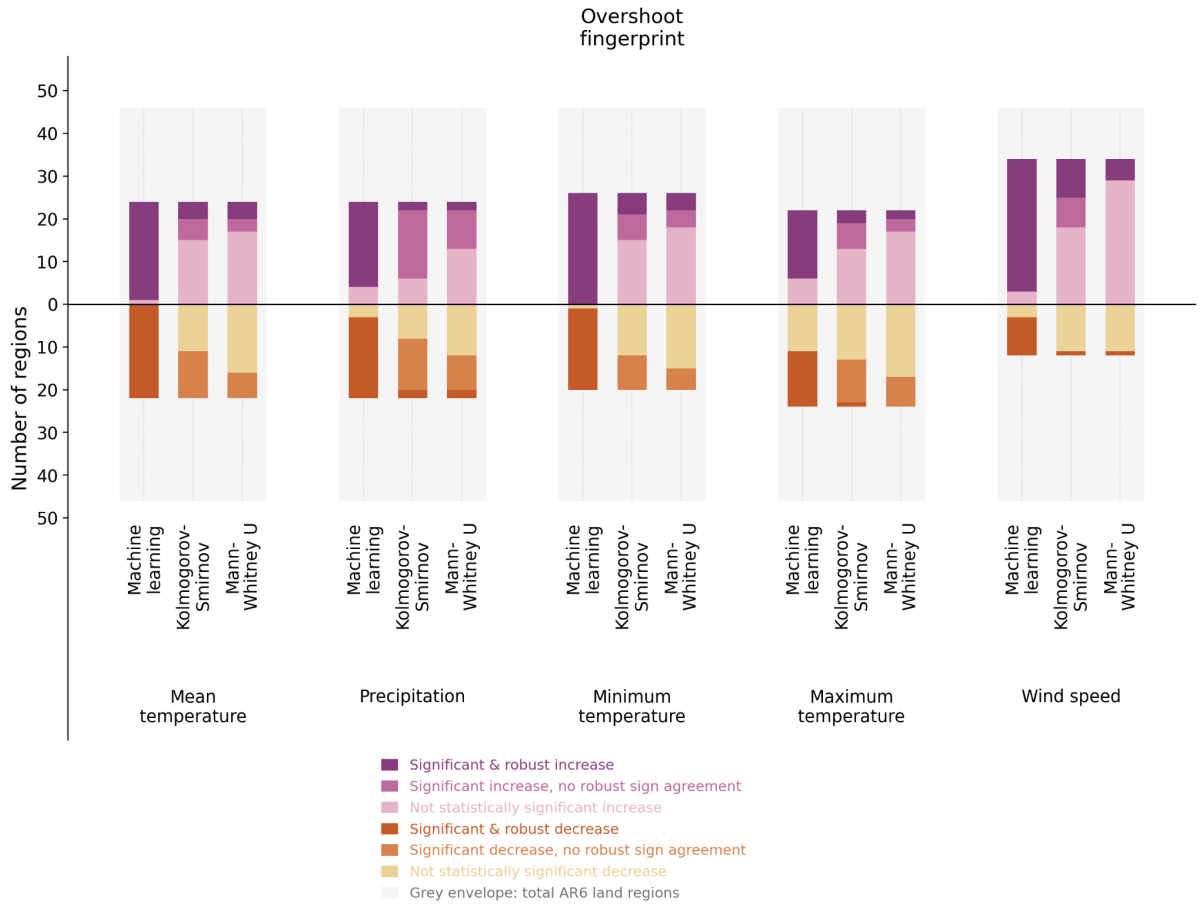

Fig. S1. Overshoot pathway fingerprint experiment with non-significant and non-robust sign

categories separated. *Similar to Fig. 2, but bars separate robust increases and robust decreases from regions that are statistically significant but lack sufficient member-wise agreement in the sign of change, and from regions that are not statistically significant. Direction is defined from the A minus B mean difference, and sign robustness is based on member-wise agreement exceeding the 60% threshold. Grey envelopes show the total number of available AR6 land regions for each variable.*

Fig. S2. Overshoot pathway fingerprint experiment with non-significant and non-robust sign categories separated, including oceans. *Similar to Fig. S1, but includes oceans.*

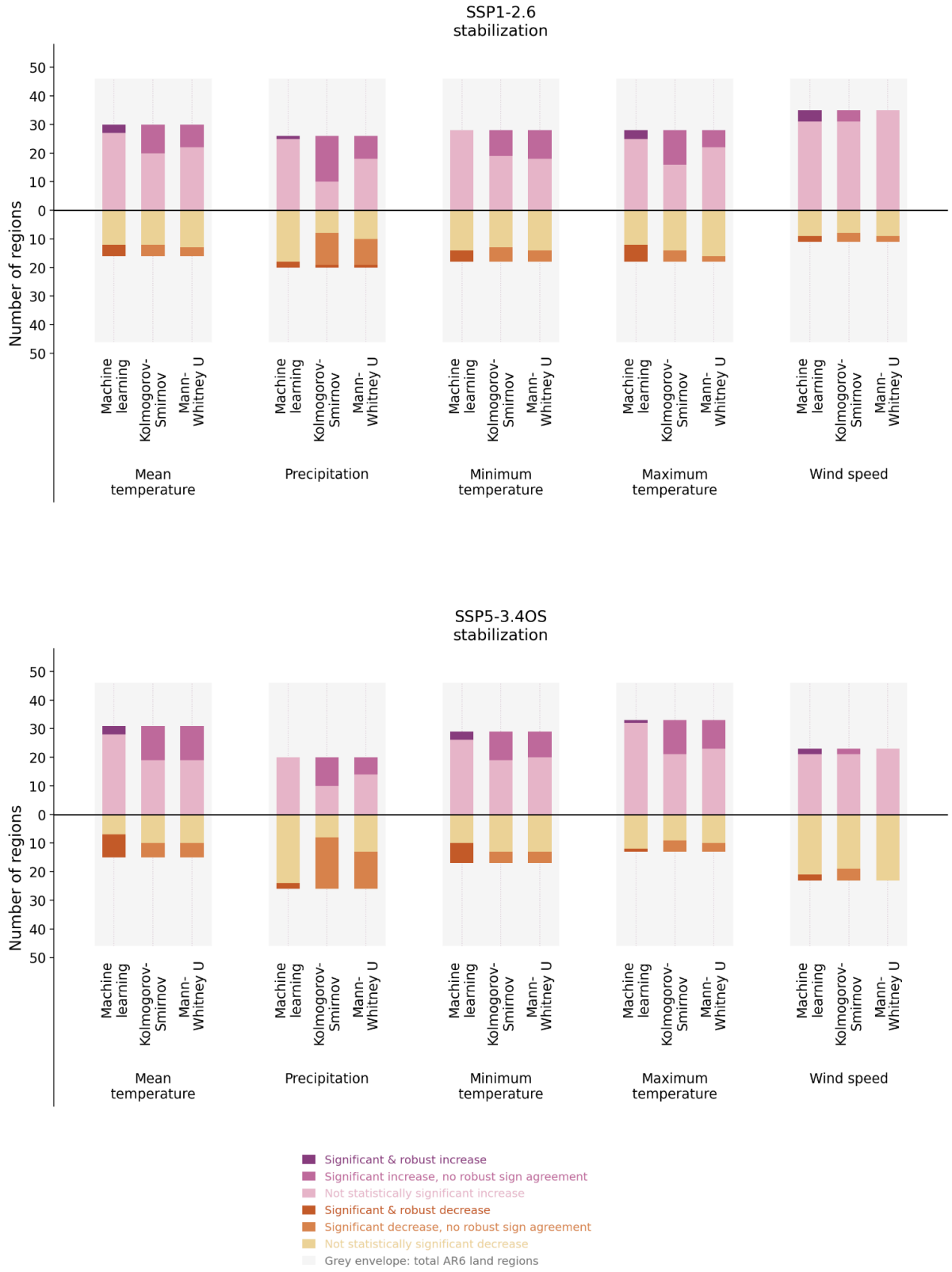

Fig. S3. Stabilization experiments with non-significant and non-robust sign categories separated. *Similar to Fig. 3, but bars separate robust increases and robust decreases from regions that are statistically significant but lack sufficient member-wise agreement in the sign of change, and from regions that are not statistically significant. Direction is defined from the A minus B mean*

difference, and sign robustness is based on member-wise agreement exceeding the 60% threshold. Grey envelopes show the total number of available AR6 land regions for each variable.

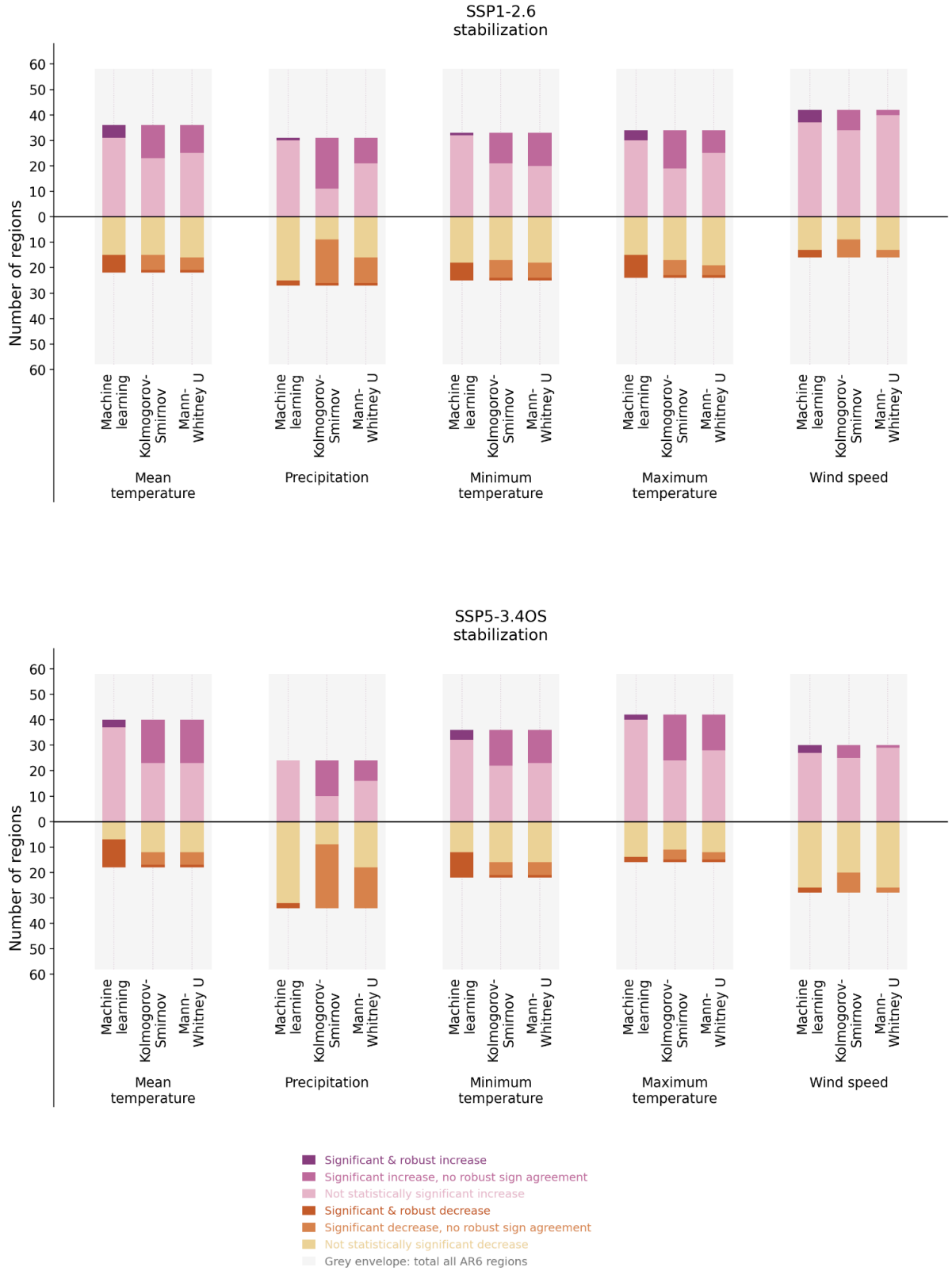

Fig. S4. Stabilization experiments with non-significant and non-robust sign categories separated, including oceans. *Similar to Fig. S3, but includes oceans.*

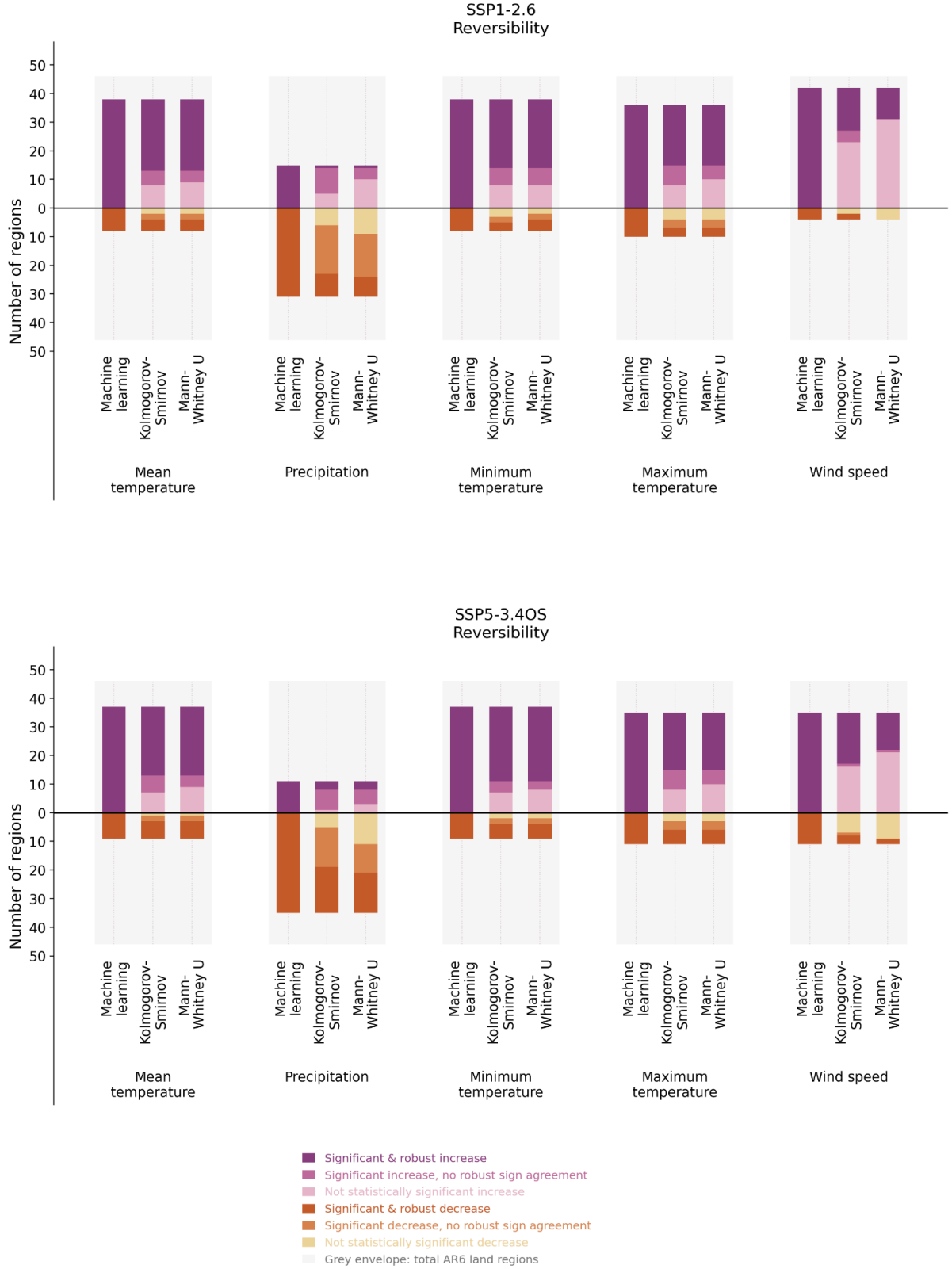

Fig. S5. Reversibility experiments with non-significant and non-robust sign categories separated. *Similar to Fig. 4, but bars separate robust increases and robust decreases from regions that are statistically significant but lack sufficient member-wise agreement in the sign of change, and*

from regions that are not statistically significant. Direction is defined from the A minus B mean difference, and sign robustness is based on member-wise agreement exceeding the 60% threshold. Grey envelopes show the total number of available AR6 land regions for each variable.

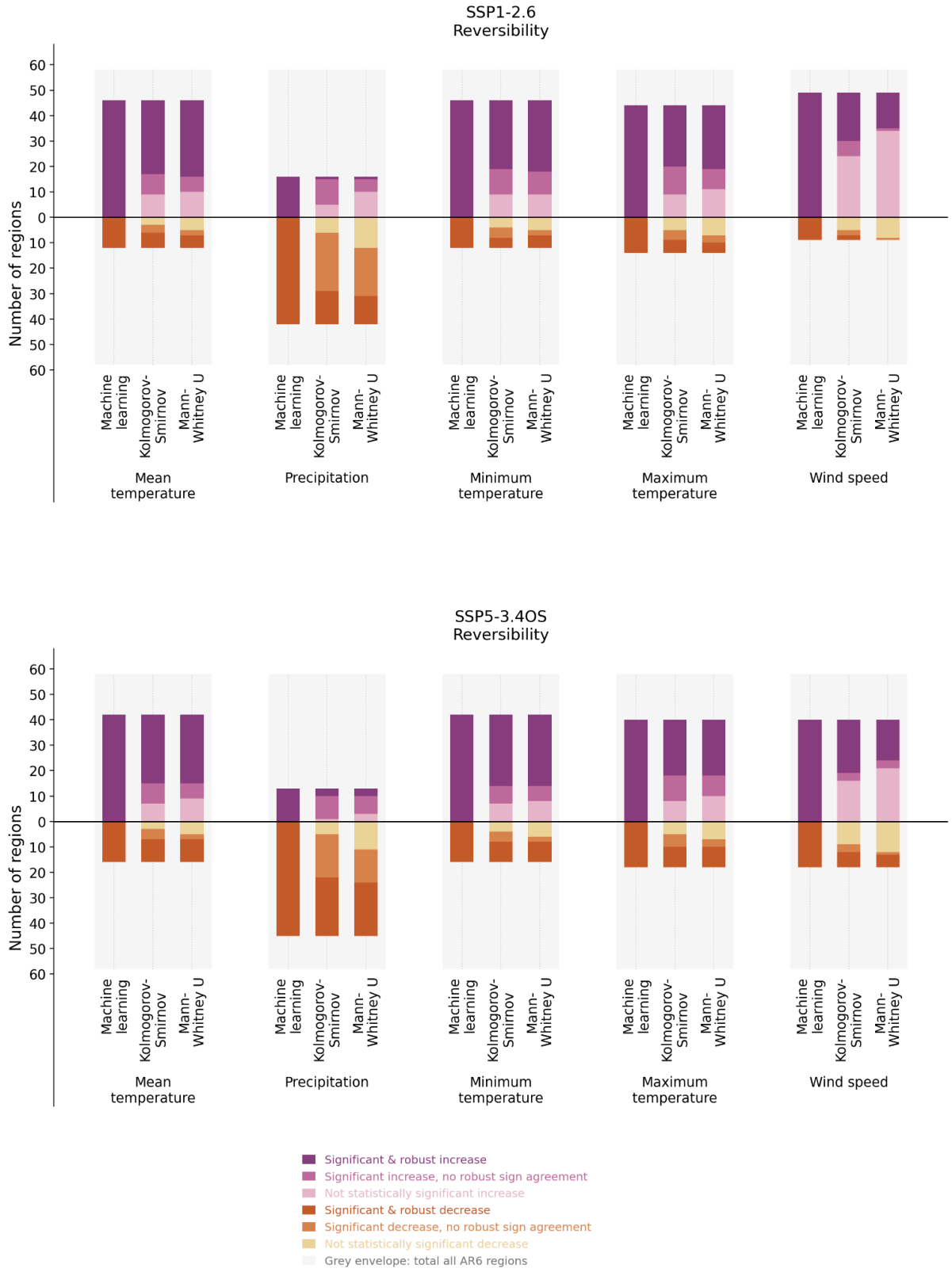

Fig. S6. Reversibility experiments with non-significant and non-robust sign categories separated, including oceans. *Similar to Fig. S5, but includes oceans.*

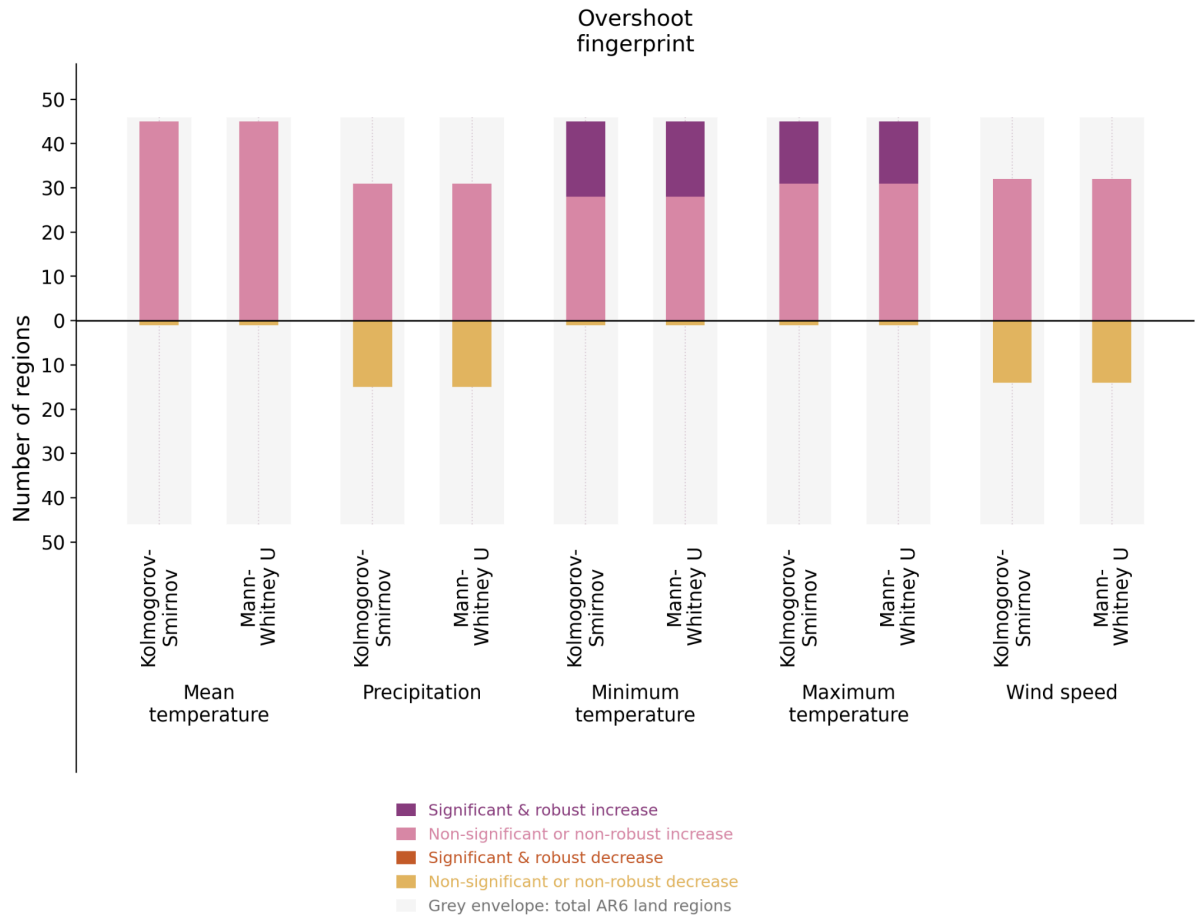

Fig. S7. Overshoot pathway fingerprint experiment with non-significant and non-robust sign categories separated using the multi-model analysis. *Similar to Fig. 2, but for the multi-model analysis. The machine learning model is excluded as it requires multiple ensemble members.*

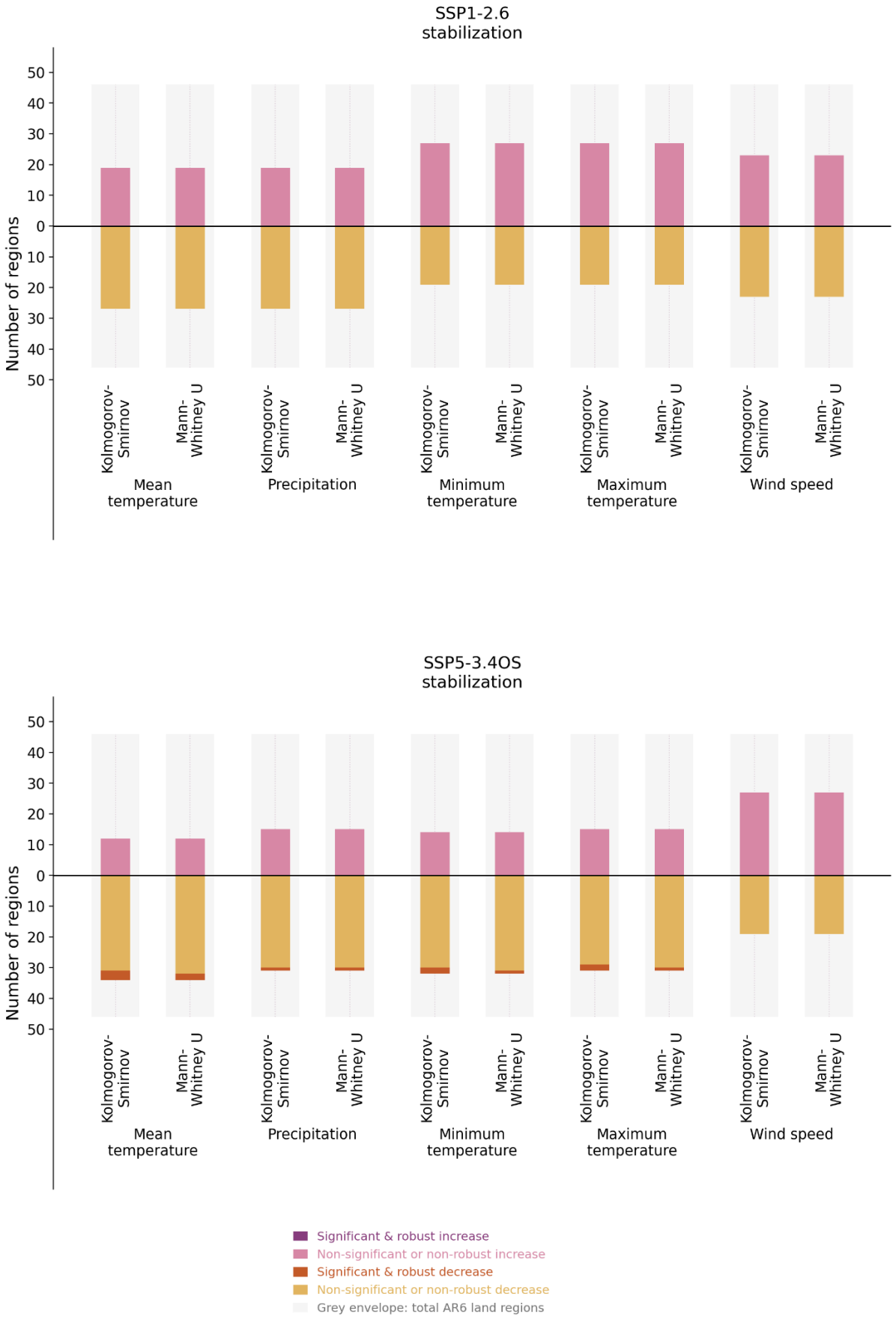

Fig. S8. Stabilization experiments with non-significant and non-robust sign categories

separated using the multi-model analysis. *Similar to Fig. 3, but for the multi-model analysis. The machine learning model is excluded as it requires multiple ensemble members.*

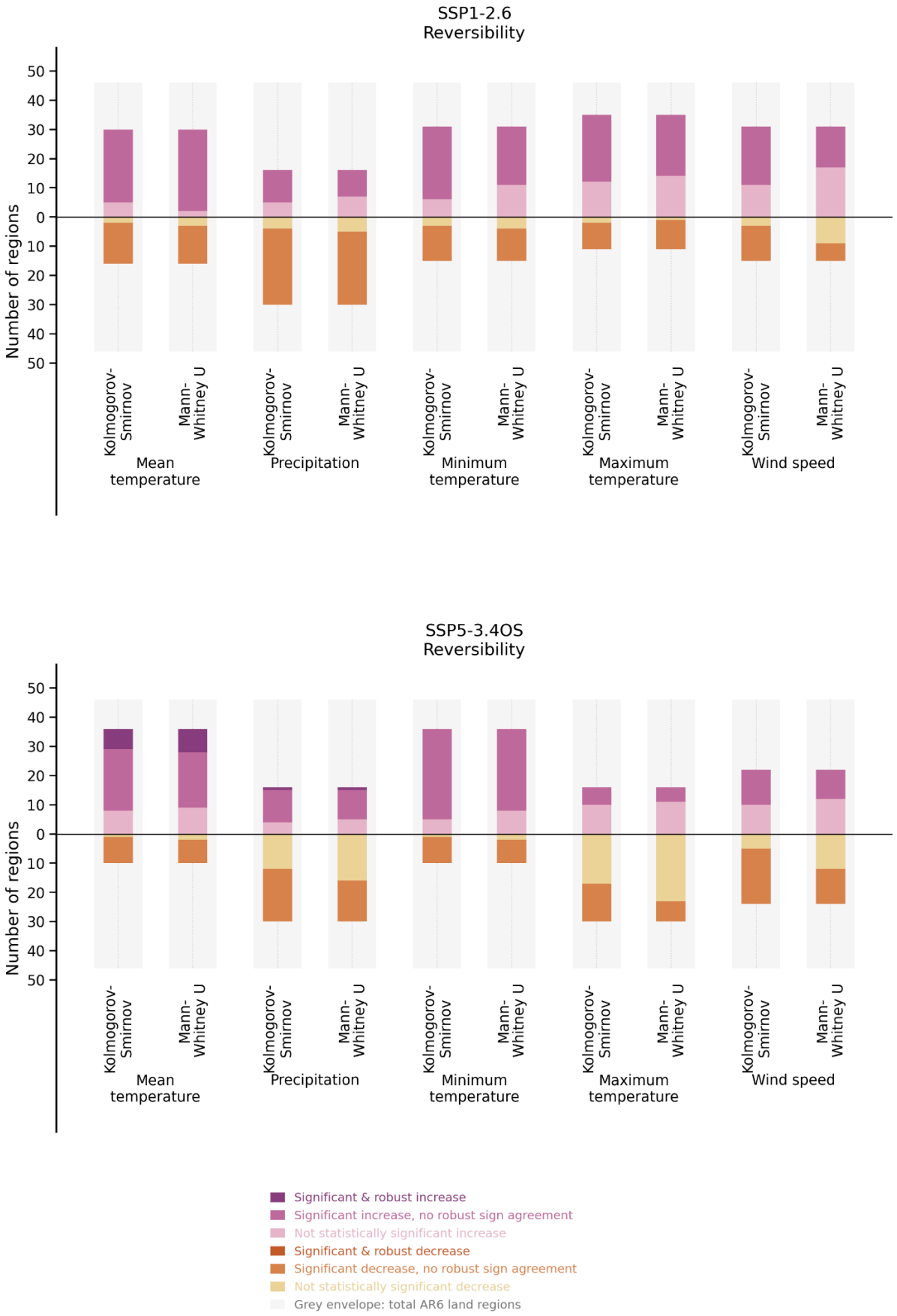

Fig. S9. Reversibility experiments with non-significant and non-robust sign categories

separated using the multi-model analysis. *Similar to Fig. 4, but for the multi-model analysis. The machine learning model is excluded as it requires multiple ensemble members.*

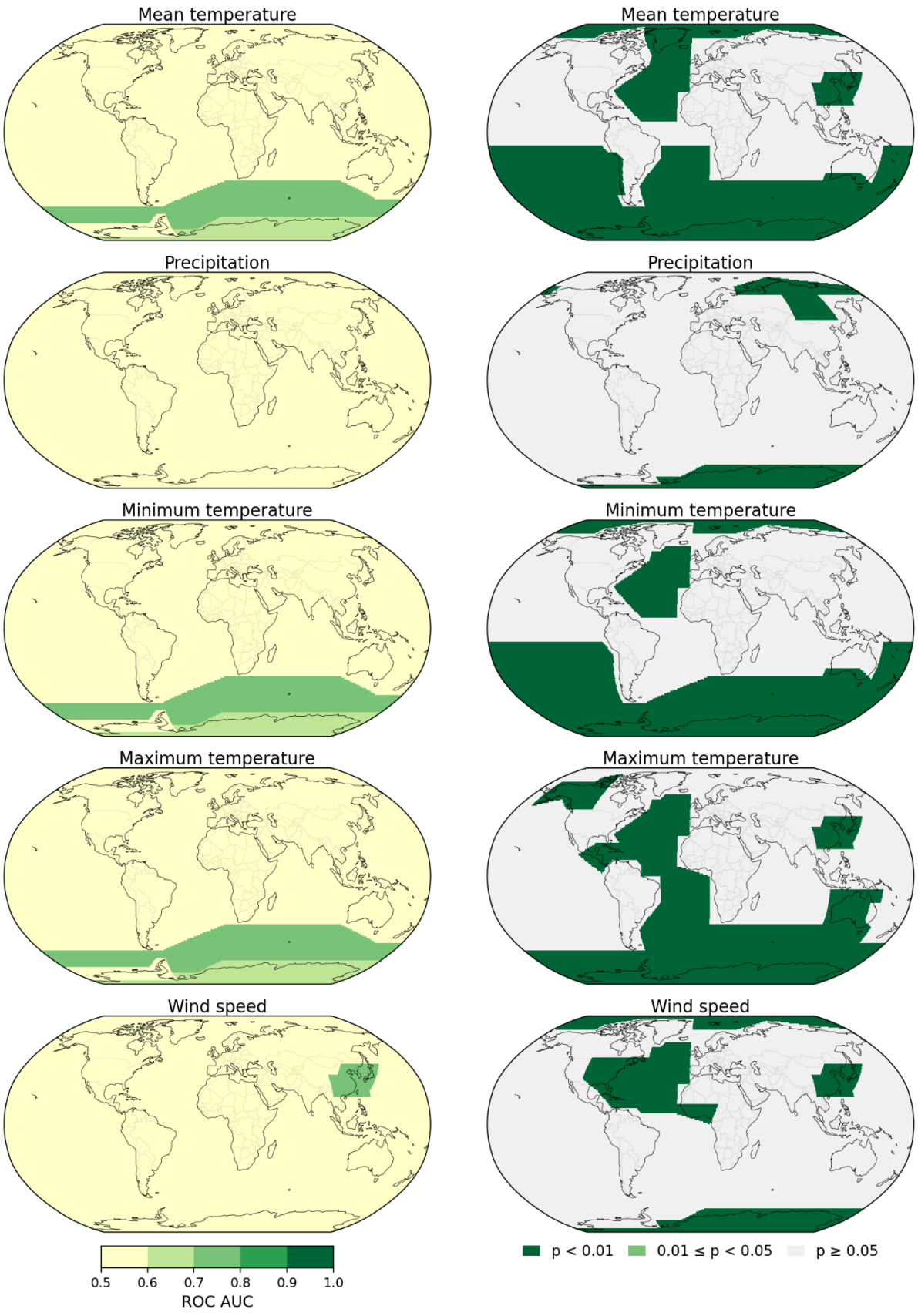

Fig. S10. Regional machine-learning performance for the SSP1-2.6 stabilization experiment. *Similar to Fig. 5, but for the SSP1-2.6 stabilization experiment.*

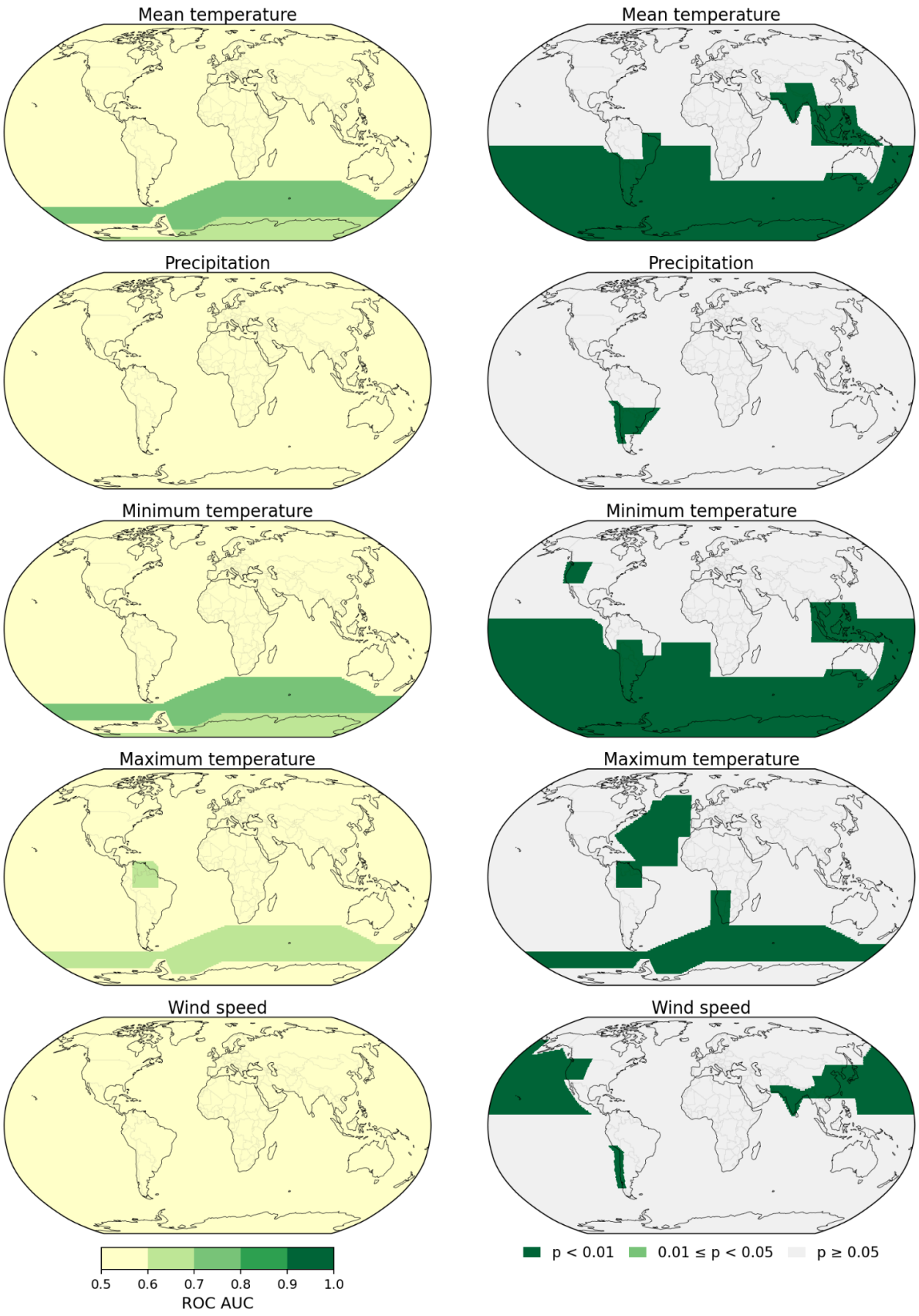

Fig. S11. Regional machine-learning performance for the SSP5-3.4OS stabilization experiment.

Similar to Fig. 5, but for the SSP5-3.4OS stabilization experiment.

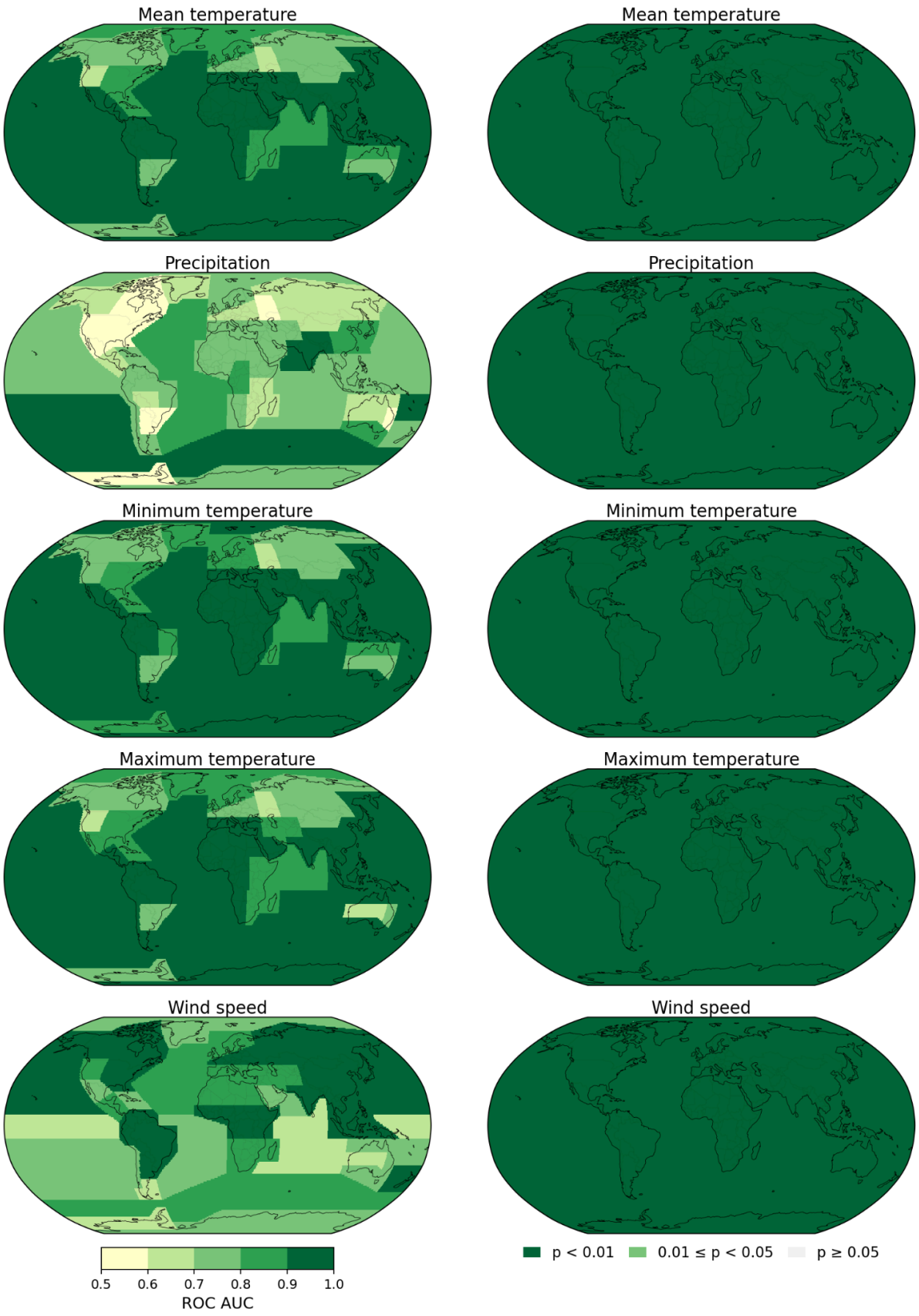

Fig. S12. Regional machine-learning performance for the SSP1-2.6 reversibility experiment. *Similar to Fig. 5, but for the SSP1-2.6 reversibility experiment.*

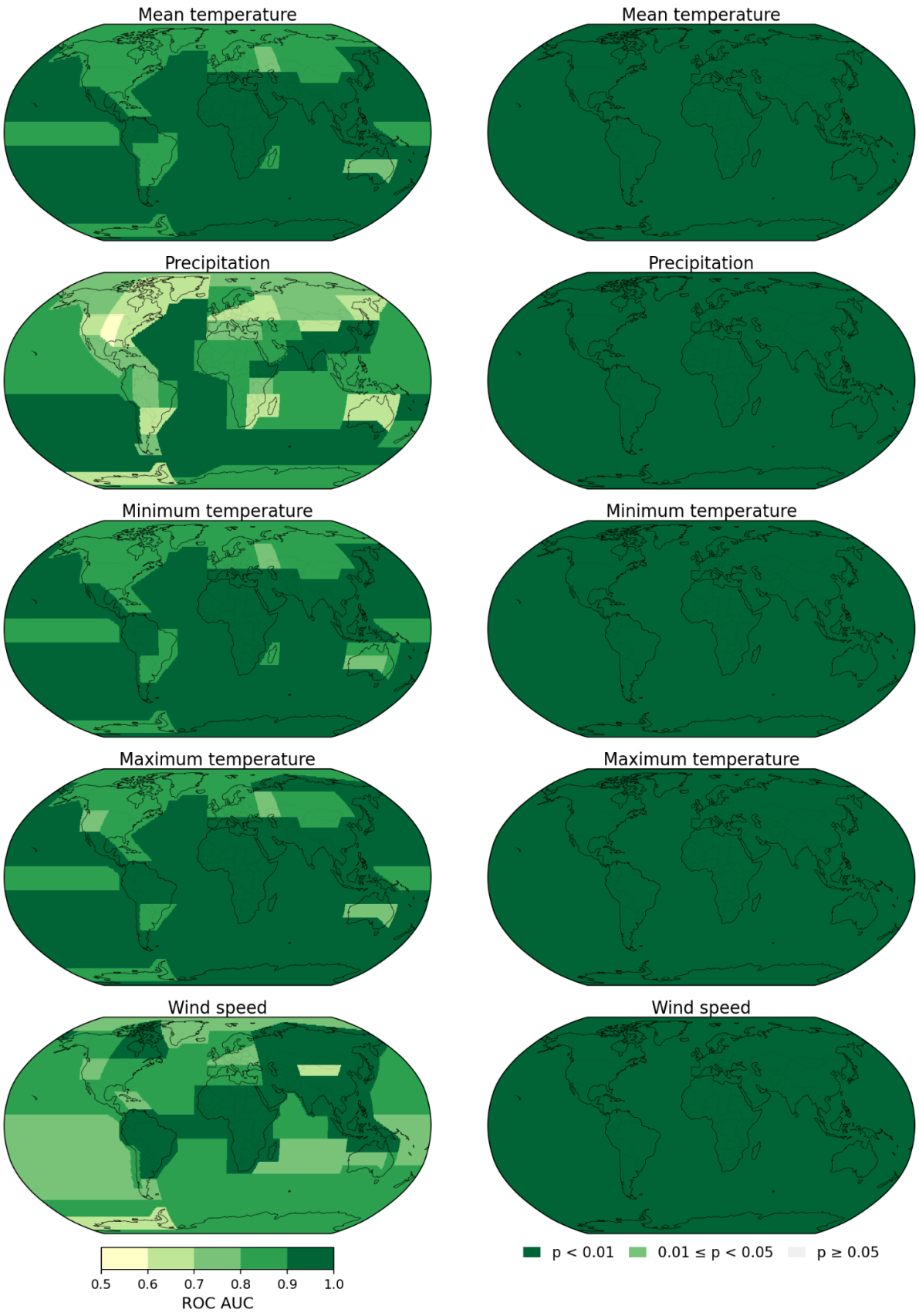

Fig. S13. Regional machine-learning performance for the SSP5-3.4OS reversibility experiment.

Similar to Fig. 5, but for the SSP5-3.4OS reversibility experiment.

References

1. E. Bevacqua, C.-F. Schleussner, J. Zscheischler, A year above 1.5 °C signals that Earth is most probably within the 20-year period that will reach the Paris Agreement limit. *Nat. Clim. Chang.* **15**, 262–265 (2025).

2. C.-F. Schleussner, *et al.*, Overconfidence in climate overshoot. *Nature* **634**, 366–373 (2024).

3. A. Reisinger, *et al.*, Overshoot: A conceptual review of exceeding and returning to global warming of 1.5°C. *Annu. Rev. Environ. Resour.* **50**, 185–217 (2025).

4. M. Tavoni, *et al.*, Implications of overshoot for climate mitigation strategies. *Nat. Clim. Chang.* **16**, 261–272 (2026).

5. J. Rogelj, A. Pirani, A. Reisinger, C.-F. Schleussner, Practical guidance towards consistent use of overshoot terminology. *Environ. Res. Lett.* **21**, 110201 (2026).

6. M. Lickley, B. B. Cael, S. Solomon, Time of steady climate change. *Geophys. Res. Lett.* **46**, 5445–5451 (2019).

7. A. D. King, *et al.*, The timing of anthropogenic emergence in simulated climate extremes. *Environ. Res. Lett.* **10**, 094015 (2015).

8. E. Hawkins, R. Sutton, Time of emergence of climate signals: TIME OF EMERGENCE OF CLIMATE SIGNALS. *Geophys. Res. Lett.* **39** (2012).

9. A. D. King, *et al.*, Exploring climate stabilisation at different global warming levels in ACCESS-ESM-1.5. *Earth Syst. Dyn.* **15**, 1353–1383 (2024).

10. P. Pfleiderer, C.-F. Schleussner, J. Sillmann, Limited reversal of regional climate signals in overshoot scenarios. *Environ. Res.: Climate* **3**, 015005 (2024).

11. P. J. Roldán-Gómez, P. De Luca, R. Bernardello, M. G. Donat, Regional irreversibility of mean and extreme surface air temperature and precipitation in CMIP6 overshoot scenarios associated with interhemispheric temperature asymmetries. *Earth Syst. Dyn.* **16**, 1–27 (2025).

12. S.-K. Kim, *et al.*, Widespread irreversible changes in surface temperature and precipitation in response to CO2 forcing. *Nat. Clim. Chang.* **12**, 834–840 (2022).

13. X. Li, K. Zickfeld, S. Mathesius, K. Kohfeld, J. B. R. Matthews, Irreversibility of marine climate change impacts under carbon dioxide removal. *Geophys. Res. Lett.* **47** (2020).

14. O. Boucher, *et al.*, Reversibility in an Earth System model in response to CO 2 concentration changes. *Environ. Res. Lett.* **7**, 024013 (2012).

15. T. Möller, *et al.*, Achieving net zero greenhouse gas emissions critical to limit climate tipping risks. *Nat. Commun.* **15**, 6192 (2024).

16. H. C. Douglas, L. E. Revell, A. King, L. J. Harrington, D. J. Frame, Effects of temperature overshoot amplitude on regional climate. *Environ. Res. Lett.* **20**, 114043 (2025).

17. T. Ziehn, *et al.*, The Australian Earth System Model: ACCESS-ESM1.5. *J. South.*

Hemisph. Earth Syst. Sci. **70**, 193–214 (2020).

18. V. Eyring, *et al.*, Overview of the Coupled Model Intercomparison Project Phase 6 (CMIP6) experimental design and organization. *Geosci. Model Dev.* **9**, 1937–1958 (2016).

19. B. C. O'Neill, *et al.*, The Scenario Model Intercomparison Project (ScenarioMIP) for CMIP6. *Geosci. Model Dev.* **9**, 3461–3482 (2016).

20. M. Iturbide, *et al.*, An update of IPCC climate reference regions for subcontinental analysis of climate model data: definition and aggregated datasets. *Earth System Science Data* **12**, 2959–2970 (2020).

21. M. Meinshausen, *et al.*, The shared socio-economic pathway (SSP) greenhouse gas concentrations and their extensions to 2500. *Geosci. Model Dev.* **13**, 3571–3605 (2020).

22. N. Swart, *et al.*, The Canadian Earth System Model version 5 (CanESM5.0.3). *Geosci. Model Dev.* (2019). https://doi.org/10.5194/GMD-12-4823-2019.

23. I. R. Simpson, *et al.*, The CESM2 single-forcing large ensemble and comparison to CESM1: Implications for experimental design. *J. Clim.* **36**, 5687–5711 (2023).

24. R. Döscher, *et al.*, The EC-Earth3 Earth System Model for the climate model intercomparison project 6. *Geoscientific Model Development Discussions* (2021).

25. R. L. Miller, *et al.*, CMIP6 historical simulations (1850–2014) with GISS-E2.1. *J. Adv. Model. Earth Syst.* **13**, e2019MS002034 (2021).

26. NASA-GISS, GISS-E2-2-G model output prepared for CMIP6 ScenarioMIP. (2021). Available at: https://doi.org/10.22033/ESGF/CMIP6.11671.

27. O. Boucher, *et al.*, Presentation and evaluation of the IPSL-CM6A-LR climate model. *J. Adv. Model. Earth Syst.* **12** (2020).

28. T. Hajima, *et al.*, Development of the MIROC-ES2L Earth system model and the evaluation of biogeochemical processes and feedbacks. *Geosci. Model Dev.* **13**, 2197–2244 (2020).

29. S. Yukimoto, *et al.*, The meteorological research institute earth system model version 2.0, MRI-ESM2.0: Description and basic evaluation of the physical component. *J. Meteorol. Soc. Japan* **97**, 931–965 (2019).

30. P. Good, *et al.*, MOHC UKESM1.0-LL model output prepared for CMIP6 ScenarioMIP ssp585. Earth System Grid Federation. https://doi.org/10.22033/ESGF/CMIP6.6405. Deposited 7 May 2019.

31. T. W. MacFarland, J. M. Yates, "Mann–Whitney U Test" in *Introduction to Nonparametric Statistics for the Biological Sciences Using R*, (Springer International Publishing, 2016), pp. 103–132.

32. A. Shmuel, N. Schwind, K. Kornhuber, R. Milo, C. Schleussner, Climate mitigation benefits emerge within a decade. *eartharxiv* (2025).

33. G. Ke, *et al.*, LightGBM: A highly efficient Gradient Boosting Decision Tree. *Neural Inf Process Syst* 3146–3154 (2017).

34. A. P. Bradley, The use of the area under the ROC curve in the evaluation of machine

learning algorithms. *Pattern Recognit.* **30**, 1145–1159 (1997).

35. A. Shmuel, O. Glickman, T. Lazebnik, A comprehensive benchmark of machine and deep learning models on structured data for regression and classification. *Neurocomputing* **655**, 131337 (2025).

36. D. McElfresh, *et al.*, When do neural nets outperform boosted trees on tabular data? *arXiv [cs.LG]* 76336–76369 (2023).

37. F. Lacroix, F. A. Burger, Y. Silvy, C.-F. Schleussner, T. L. Frölicher, Persistently elevated high-latitude ocean temperatures and global sea level following temporary temperature overshoots. *Earths Future* **12** (2024).

38. J. Schwinger, A. Asaadi, N. Goris, H. Lee, Possibility for strong northern hemisphere high-latitude cooling under negative emissions. *Nat. Commun.* **13**, 1095 (2022).

39. Y.-H. Lee, S.-W. Yeh, G. Wang, S.-Y. Song, S.-I. An, Deep ocean control of global temperature after net-zero emissions. *Nat. Geosci.* **19**, 406–409 (2026).

40. S.-Y. Kim, *et al.*, Hemispherically asymmetric Hadley cell response to CO2 removal. *Sci. Adv.* **9**, eadg1801 (2023).

41. C. Liu, *et al.*, Hysteresis of the El Niño-Southern Oscillation to CO_2 forcing. *Sci. Adv.* **9**, eadh8442 (2023).

42. S. Paik, S.-I. An, S.-K. Min, A. D. King, J. Shin, Hysteretic behavior of global to regional monsoon area under CO_2 ramp-up and ramp-down. *Earths Future* **11** (2023).

43. G. Pathirana, *et al.*, Increase in convective extreme El Niño events in a CO_2 removal scenario. *Sci. Adv.* **9**, eadh2412 (2023).

44. N. J. Steinert, J. Schwinger, R. Chadwick, J.-S. Kug, H. Lee, Irreversible land water availability changes from a potential ITCZ shift during temperature overshoot. *Earths Future* **13** (2025).

45. B. H. Samset, *et al.*, Climate impacts from a removal of anthropogenic aerosol emissions. *Geophys. Res. Lett.* **45**, 1020–1029 (2018).

46. G. G. Persad, K. Caldeira, Divergent global-scale temperature effects from identical aerosols emitted in different regions. *Nat. Commun.* **9**, 3289 (2018).

47. A. Borowiak, *et al.*, Projected global temperature changes after net zero are small but significant. *Geophys. Res. Lett.* **51** (2024).